https://doi.org/10.5194/egusphere-2026-512
Preprint. Discussion started: 30 April 2026

Subtropical Extreme Heatwave Dynamics in the Intermediate-Complexity Atmospheric Model Aeolus 2.0

Sullyandro O. Guimarães[1,2], Masoud Rostami[1,3], Stefan Petri[1]

[1]Potsdam Institute for Climate Impact Research (PIK), Member of the Leibniz Association, Potsdam, Germany
[2]University of Potsdam, Potsdam, Germany
[3]Laboratoire de Météorologie Dynamique (LMD), Sorbonne University (SU), Ecole Normale Supérieure (ENS), Paris, France

Correspondence to: Sullyandro O. Guimarães (sullyandro@pik-potsdam.de)

Abstract. Heatwaves in the subtropical and mid-latitude regions, which arise from localized heating can ripple through the atmosphere and persist for weeks, yet the mechanisms behind this chain of events remain difficult to disentangle. Here we use the Aeolus 2.0 model, which is a moist-convective thermal rotating shallow-water (mcTRSW) framework of intermediate complexity, to explore how buoyancy anomalies evolve under both dry and moist conditions, innovatively including background effects to enhance realism. We find that localized heating sets off a rapid atmospheric adjustment: air converges near the surface, diverges aloft, and quickly organizes into paired cyclonic (lower layer) and anticyclonic circulations (upper layer). Earth's rotation then distorts these structures, producing asymmetries, spiral rainbands, and rainband-driven feedbacks. Moist convection greatly amplifies this response by releasing latent heat, which fuels sustained instability and rainfall organization. Inertia–gravity waves emerge as a key pathway for redistributing heat and momentum, while Rossby waves and beta gyres gradually reshape anomalies, tilting them poleward and breaking them into smaller vortices. The simulations also reproduce well-known observational signatures, including comma-shaped water vapor patterns and mesoscale vortices. Together, these results show how a simple localized heat source can trigger a cascade of atmospheric responses that link convection, wave dynamics, and large-scale circulation. By capturing these processes, Aeolus 2.0 provides a bridge between theoretical frameworks and full climate models, offering new insight into the dynamics that sustain extreme heatwaves in a warming world.

Keywords: Moist-convective Thermal rotating shallow water (mcTRSW) model, Heatwaves, Aeolus 2.0, Extreme forcings.

1 Introduction

Heatwaves are occurring more often and with greater intensity around the globe, particularly impacting subtropical and mid-latitude regions. Recent instances of such heatwaves have been recorded in North America, Europe, and Asia (Gao et al., 2023, Wang et al., 2025). Their origins are based in different physical causes, as those formed from the atmosphere, like moisture and radiation, and other from the surface drivers. Sometimes, these causes can mix and create complex effects, a combination of atmospheric dynamics and land-surface interactions, with feedback mechanisms that can amplify their intensity and duration

https://doi.org/10.5194/egusphere-2026-512
Preprint. Discussion started: 30 April 2026

(Petoukhov et al., 2013; Guimarães et al., 2024; Miralles et al., 2019; Zeppetello et al., 2022; Hao et al., 2022, Barriopedro et al., 2023).

Blocking circulation patterns are often mentioned as the phenomena responsible for the association of persistent atmospheric high-pressure anomalies and linked heatwaves (Schaller et al, 2018; Kautz et al., 2022; Nabizadeh et al., 2021; Rouges et al., 2023). In this study, the term heatwaves is used in a connotation to describe the phenomenon involving the gradual formation and sustained presence of large-scale, localized regions of positive buoyancy. These regions develop due to elevated potential temperatures over several days and are analyzed within a framework influenced by the background zonal flow. By using an atmospheric model of intermediate complexity, we are able to isolate and better understand the key physical processes that drive the emergence and evolution of these anomalies, as will be discussed in the model description session. A defining feature of these buoyant structures is their persistence - they are capable of remaining active and hold over multiple consecutive days, highlighting their significance in the broader context of extreme weather patterns.

Limited studies have provided detailed simulations or conceptual models that capture these atmospheric blocking structures effectively, commonly identified by the appearance of ridge-like high-pressure systems within upper-tropospheric geopotential-height contours (Sousa et al., 2021; Schemm and Sprenger, 2019; Kautz et al., 2021). In response to this gap, the present work investigates whether extreme surface heating can contribute to the development of atmospheric ridges in the upper troposphere, building on theoretical understanding of the atmospheric response to thermal forcing and on recent modeling and observational studies that link strong diabatic or surface heating with the amplification of upper-level ridges (Hoskins and Karoly, 1981; Zhang and Wang, 2018; Rostami et al., 2023; Liu et al., 2025).

From our findings, upper-tropospheric ridges can emerge in tandem with localized surface warming events. These simultaneous developments are linked to surface-induced heating, which gives rise to a thermal low-pressure zone and associated cyclonic circulation near the surface, acting in contrast to the anticyclonic conditions in the upper layer. Modelled and observational evidence support the coexistence of these lower and upper-atmospheric features (Pfahl and Wernli, 2012; Rostami et al., 2023). It is worth emphasizing that a comprehensive theoretical framework capable of fully explaining all facets of heatwaves has yet to be established. Rather than replicating real-world heatwave events, this research aims to explore the fundamental evolution of buoyancy-driven anomalies under the influence of the innovative background wind velocity effects, baroclinicity, moist convection, and the full Coriolis force, in order to capture their essential dynamics.

In simplified atmospheric conditions that exclude moisture processes, geostrophic balance tends to form through the generation of horizontal temperature contrasts following localized heating. Such "dry" environments are governed by adiabatic dynamics, where the absence of phase transitions ensures total energy conservation, as described by Holton and Hakim (2013). In contrast, real atmospheric environments are shaped by more complex, non-adiabatic processes that depend heavily on vertical layering, atmospheric stability, wind shear, and, critically, the influence of moist convection. Moist convection significantly alters the

https://doi.org/10.5194/egusphere-2026-512
Preprint. Discussion started: 30 April 2026

adjustment dynamics in subtropical and mid latitude systems, exerting a strong influence on both short-term weather developments and broader climate behavior.

Gaining insight into the behavior of these buoyancy anomalies is essential for improving our ability to anticipate atmospheric responses under a range of weather and climate scenarios. The moist-convective Thermal Rotating Shallow Water (mcTRSW) model serves as a valuable tool in this effort, offering a simplified framework to investigate how temperature variations, moisture content, and large-scale atmospheric circulation interact in shaping these dynamic processes (Kurganov et al., 2020; Rostami et al., 2022; 2023). In this study, we use the stand-alone version of the atmospheric model Aeolus 2.0 (Rostami et al., 2024a; 2025) to investigate the dynamics of localized extreme heatwaves in the subtropical atmosphere under both dry and moist-convective scenarios. See Guimarães et al. (2025) for the Aeolus 2.0 code and data specific to this study.

2 Methodology

2.1 Model Description

To better understand how buoyancy anomalies influence atmospheric behavior -particularly during extreme heat events - we rely on a modeling framework that combines conceptual clarity with physical robustness. The historical foundation of our approach lies in the moist-convective Rotating Shallow Water (mcRSW) model, which offers a robust theoretical basis for simulating moist processes in the atmosphere. This model incorporates key features such as phase transitions of water vapor and the associated latent heat release, following the foundational principles established by Gill (1982) and further developed by Bouchut et al. (2009) and Lambaerts et al. (2011ab; 2012). The mcRSW framework represents the evolution of column-integrated humidity and the impact of condensation in a consistent and simplified manner, making it well-suited for idealized studies. Over time, the model has been refined to include additional moist-convective processes such as vaporization, precipitation, and precipitable water (Rostami and Zeitlin, 2018), and it has been applied successfully in numerous studies of large-scale atmospheric jets and vortices on Earth and other planets. Building on this foundation, we apply the mcTRSW model Aeolus 2.0 (Rostami et al., 2024a; 2025a) in our experiments. This tool developed at the Potsdam Institute for Climate Impact Research (PIK) allows us to explore the dynamics of subtropical and mid-latitude heatwaves under both dry and moist-convective conditions, offering new insights into how temperature, moisture, and circulation interact to shape extreme events.

The dynamical core of Aeolus 2.0 is constructed upon a multi-layer formulation of the mcTRSW model. The underlying principles and mathematical formulation of the multi-layer TRSW system, including its capacity to represent vertical structure and thermodynamic interactions, are thoroughly presented in Rostami et al. (2025a; 2025b). Unlike conventional shallow water models that are typically based on the assumptions of layer homogeneity, incompressibility, and hydrostatic equilibrium, the TRSW framework relaxes these constraints by allowing for horizontal variability in thermodynamic and material properties across stratified layers. This enhanced representation is achieved through a vertical integration of the atmospheric primitive

https://doi.org/10.5194/egusphere-2026-512
Preprint. Discussion started: 30 April 2026

equations, formulated within a pseudo-height isobaric coordinate system. Such a configuration enables the model to more accurately capture the vertical structure and thermodynamic gradients of the atmosphere (see **Fig. 1**), thereby extending its applicability to a broader range of dynamical and thermodynamical regimes.

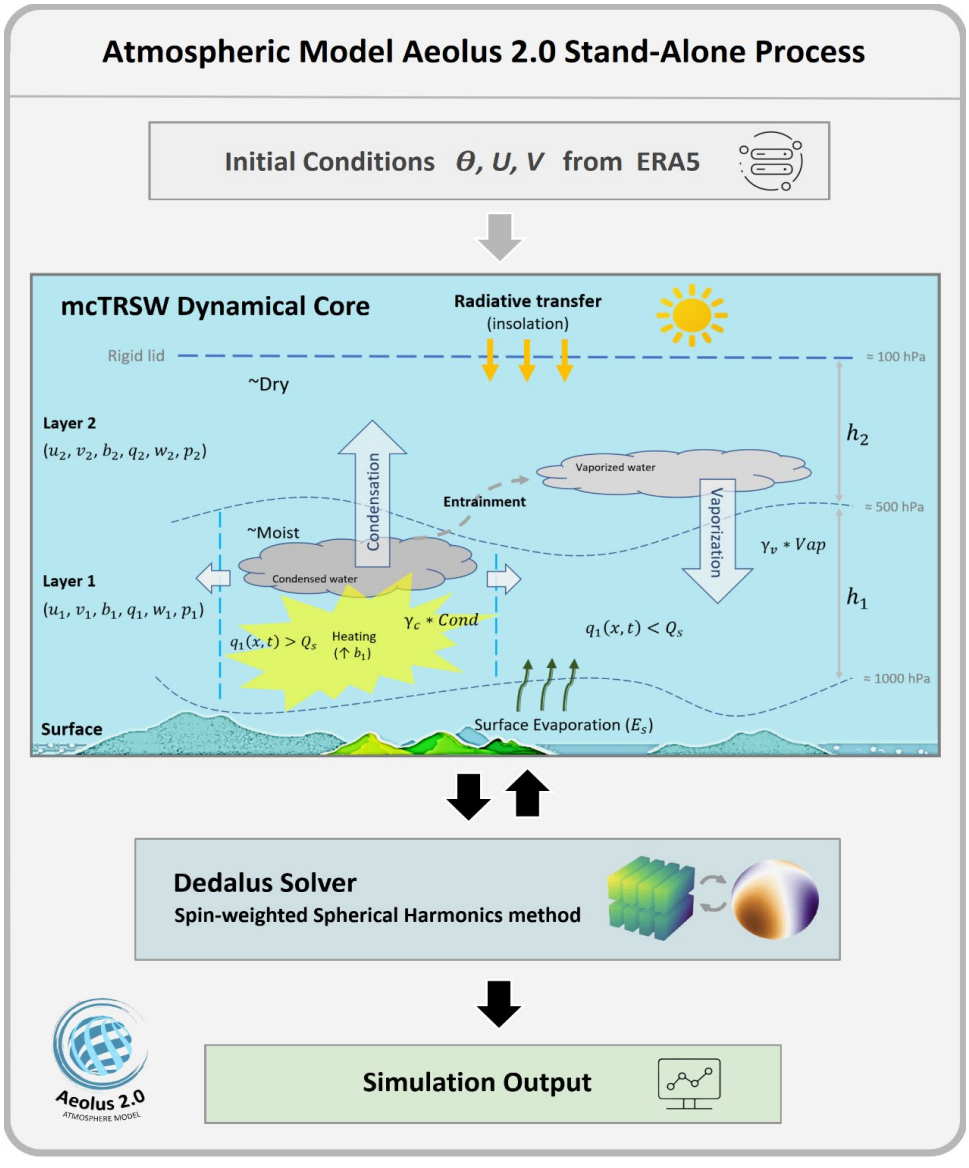

Figure 1: Schematic illustration of the Aeolus 2.0 model stand-alone process. Elements in here were adapted from Rostami et al. (2024a) and Dedalus Project (*dedalus-project.org*, Burns et al., 2020). Where: u and v (wind velocity); b (buoyancy); q (water vapor); w (precipitable water); p (pressure); and h (layer thickness); Q_s (saturation vapor pressure); Vap (vaporization); $Cond$ (condensation); $\gamma_c * Cond$ and $\gamma_v * Vap$ (Entrainment terms); and θ (potential temperature).

https://doi.org/10.5194/egusphere-2026-512
Preprint. Discussion started: 30 April 2026

The model offers a robust and coherent representation of horizontal potential temperature gradients and their temporal evolution under the influence of moist convection. This is achieved through a formulation that remains both physically consistent and computationally transparent. A key strength of the mcTRSW framework lies in its ability to fully capture the nonlinear characteristics of moist convection, integrating essential processes such as latent heat release, phase transitions of water vapor, and the dynamic modulation of buoyancy. These capabilities enable the model to explore the underlying mechanisms of extreme weather phenomena, including surface heat fluxes and the central role of moist convective activity.

The two-layer version of the Aeolus 2.0 mcTRSW model is built upon a set of fundamental equations that describe its behavior and dynamics. These governing equations, thoroughly explained in Rostami et al. (2023; 2024a; 2025a; 2025b) and Cao et al. (2025), form the foundation of the model and are summarized below to provide a clear understanding of the system's core structure and functionality. Additional flux-form equations implemented in Aeolus 2.0, following Cao et al. (2025), are provided in the **Supplementary Material**.

Nondimensionalization is applied to simplify the system dynamics, with the barotropic equatorial Rossby deformation radius (L_d) serving as the characteristic horizontal length scale (L). Here, $L_d = (\sqrt{gH}/\beta)^{1/2}$, $H = H_1 + H_2$ represents the total unperturbed layer depth, H_i is the resting-state values for thickness, g is the gravitational acceleration, and β is the meridional gradient of the Coriolis parameter. The scaling relations for velocity components (u, v) and time (t) are given by: $L \sim L_d$, $(u, v) \sim \beta L_d^2$, and $t \sim 1/(\beta L_d)$, as enlightened in Rostami et al. (2025a).

$$(\partial_t + \boldsymbol{v}_1 \cdot \boldsymbol{\nabla})\boldsymbol{v}_1 + f\hat{\boldsymbol{z}} \times \boldsymbol{v}_1 = -\langle \boldsymbol{\nabla} p_1 \rangle \tag{1a}$$

$$(\partial_t + \boldsymbol{v}_2 \cdot \boldsymbol{\nabla})\boldsymbol{v}_2 + f\hat{\boldsymbol{z}} \times \boldsymbol{v}_2 = -\langle \boldsymbol{\nabla} p_2 \rangle - \frac{(1-\gamma)}{b_2 h_2}(\boldsymbol{v}_2 - \boldsymbol{v}_1)(\mathcal{C} - \mathcal{D}) \tag{1b}$$

$$\partial_t h_1 + \boldsymbol{\nabla} \cdot (h_1 \boldsymbol{v}_1) = \frac{1}{b_1}[(1-\gamma)(-\mathcal{C} + \mathcal{D}) - (1-\gamma^*)\mathbb{F}_1] \tag{1c}$$

$$\partial_t h_2 + \boldsymbol{\nabla} \cdot (h_2 \boldsymbol{v}_2) = \frac{1}{b_2}[(1-\gamma)(+\mathcal{C} - \mathcal{D}) - (1-\gamma^*)\mathbb{F}_2] \tag{1d}$$

$$\partial_t b_1 + \boldsymbol{v}_1 \cdot \boldsymbol{\nabla} b_1 = \frac{1}{h_1}[(+\mathcal{C} - \mu\mathcal{E}_s) + \mathbb{F}_2] \tag{1e}$$

$$\partial_t b_2 + \boldsymbol{v}_2 \cdot \boldsymbol{\nabla} b_2 = \frac{1}{h_2}[(-\mathcal{C} + \mathcal{D}) + \mathbb{F}_2] \tag{1f}$$

$$\partial_t q_1 + \boldsymbol{\nabla} \cdot (q_1 \boldsymbol{v}_1) = -\mathcal{C} + \mathcal{E}_s \tag{1g}$$

$$\partial_t q_2 + \boldsymbol{\nabla} \cdot (q_2 \boldsymbol{v}_2) = +\mathcal{C} - \mathcal{D} \tag{1h}$$

https://doi.org/10.5194/egusphere-2026-512
Preprint. Discussion started: 30 April 2026

The model applies a Lagrangian (or material) derivative to describe the time evolution of atmospheric quantities within each layer. This derivative is expressed as $\partial/\partial t + \boldsymbol{v}_i \cdot \boldsymbol{\nabla}$, where $\boldsymbol{v}_i = (u_i,\ v_i)$ denotes the vertically-averaged horizontal velocity vector in each layer i, and $\boldsymbol{\nabla}$ represents the horizontal gradient operator. This formulation allows the model to track changes not only over time but also as air parcels move horizontally, capturing the essential dynamics of advection and temporal evolution in a layered atmospheric system. Each layer's thickness is represented by h_i, with layers numbered sequentially from the surface upward, as presented in **Fig. 1**.

To define the structure of the pressure gradient terms in the governing equations, we specify the relevant velocity and pressure-related quantities for each model layer. In this formulation, $\langle \boldsymbol{\nabla} p_i \rangle = \boldsymbol{\nabla} \tilde{p}_i - \tilde{h}_i \boldsymbol{\nabla} b_i$ represents the vertically-averaged horizontal gradient of the pressure field. For the 2 layers schema, the lower layer gradient is $\langle \boldsymbol{\nabla} p_1 \rangle = (1/2) h_1 \boldsymbol{\nabla} b_1 + b_1 \boldsymbol{\nabla}(h_b + h_1 + h_2)$, and in the upper layer $\langle \boldsymbol{\nabla} p_2 \rangle = \boldsymbol{\nabla}(h_1 b_1) + (1/2) h_2 \boldsymbol{\nabla} b_2 + b_2 \boldsymbol{\nabla}(h_b + h_2)$, where h_b is a bottom topography height, $\tilde{p}_1 = (h_b + h_1 + h_2) b_1$, $\tilde{p}_2 = h_1 b_1 + (h_b + h_2) b_2$, $\tilde{h}_1 = h_b + (1/2) h_1 + h_2$, and $\tilde{h}_2 = h_b + (1/2) h_2$.

To characterize buoyancy within a given layer (b_i), the model uses a vertically averaged formulation $b_i = g \overline{\theta}_i / \theta_s$, where $\overline{\theta}_i$ is the vertically-averaged potential temperature in layer i, and θ_s represents a reference surface-level potential temperature.

The model further includes several moisture-related and thermodynamic parameters. These include $\mathcal{C}$, which accounts for condensed liquid water in the lower layer (also referred as CLWC), playing in upward motion; $\mathcal{D}$, downward convective flux term; $\mathcal{E}_s$, representing surface evaporation through a bulk aerodynamic formula; μ, an amplitude equivalence term between $\mathcal{C}$ and $\mathcal{E}_s$; and γ and γ^*, which quantify the thermodynamic contributions of latent heat from condensation and radiative cooling (Newtonian relaxation), respectively. These parameters can vary with vertical level. In complement, external thermal forcings are incorporated in the term $\mathbb{F}_i$, including insolation and a Newtonian cooling term.

The rotational and directional effects are included through the Coriolis parameter f and a vertical unit vector $\hat{\boldsymbol{z}}$ to define orientation in the model domain.

It is important to point out that, in **Equations (1a-h)**, we simplify the system by assuming that the buoyancy term (b_i) is much larger than the moisture term (q_i/h_i), where q_i refers to the vertically integrated specific humidity. The model also includes the effects of precipitable water and the vaporization of condensed water. The Cloud Liquid Water Content (CLWC) is parameterized using the Betts–Miller convective adjustment scheme (Betts and Miller, 1986), which provides a simplified yet effective representation of moist processes. The numerical implementation relies on the Dedalus framework (Lecoanet et al., 2019; Vasil et al., 2019), offering a flexible, high-precision platform for solving the partial differential equations governing geophysical fluid dynamics.

https://doi.org/10.5194/egusphere-2026-512
Preprint. Discussion started: 30 April 2026

In an adiabatic setting, the thermogeostrophic balance can be described using the following **Equations (2a-b)**. A constant geopotential level is assumed at the lower boundary. Under the following scaling, the thickness and buoyancy fields are expressed as: $\boldsymbol{v}_i \sim U$, $(x,y)\sim L$, $h_i \sim H_0(\delta_i + \lambda\eta_i)$, $b_i \sim B_0(B_i + \lambda b_i')$, $f \sim f_0$, where U is the characteristic horizontal velocity scale, $\delta_i = H_i/H_0$ is the thickness in nondimensional scale, H_0 is thickness at rest, η_i is the deviation of the δ_i thickness, B_0 is the buoyancy at rest, B_i is the buoyancy resting state, b_i' is the buoyancy perturbation, ϕ is the latitude, λ is a small nondimensional parameter, f_0 denotes the Coriolis parameter at a reference latitude, and $R_0 = \frac{U}{f_0 L} \sim \lambda$ is the Rossby number.

$$R_0 \frac{d\boldsymbol{v}_1}{dt} + sin(\phi)\,\hat{\boldsymbol{z}} \times \boldsymbol{v}_1 = -\frac{Bu\lambda}{R_0}\left(\frac{\delta_1}{2}\boldsymbol{\nabla} b_1' + B_1 \boldsymbol{\nabla}(\eta_1 + \eta_2)\right) \tag{2a}$$

$$R_0 \frac{d\boldsymbol{v}_2}{dt} + sin(\phi)\,\hat{\boldsymbol{z}} \times \boldsymbol{v}_2 = -\frac{Bu\lambda}{R_0}\left(\delta_1 \boldsymbol{\nabla} b_1' + \frac{\delta_2}{2}\boldsymbol{\nabla} b_2' + B_1 \boldsymbol{\nabla}\eta_1 + B_2 \boldsymbol{\nabla}\eta_2\right) \tag{2b}$$

The evolution equations of a two-layer TRSW model in a "dry" atmosphere are defined ahead - **Equations (3a-f)**, to examine the dynamics underlying positive buoyancy anomalies and their connection to pressure perturbations. This formulation helps to clarify how gradients in potential temperature are linked to pressure anomalies within a simplified dry environment.

$$(\partial_t + \boldsymbol{v_1}\cdot\boldsymbol{\nabla})\boldsymbol{v}_1 + f\hat{z} \times \boldsymbol{v}_1 = -\langle \boldsymbol{\nabla} p_1 \rangle \tag{3a}$$

$$(\partial_t + \boldsymbol{v_2}\cdot\boldsymbol{\nabla})\boldsymbol{v_2} + f\hat{z} \times \boldsymbol{v}_2 = -\langle \boldsymbol{\nabla} p_2 \rangle \tag{3b}$$

$$\partial_t h_1 + \boldsymbol{\nabla}\cdot(h_1 \boldsymbol{v_1}) = 0 \tag{3c}$$

$$\partial_t h_2 + \boldsymbol{\nabla}\cdot(h_2 \boldsymbol{v_2}) = 0 \tag{3d}$$

$$\partial_t b_1 + \boldsymbol{v_1}\cdot\boldsymbol{\nabla} b_1 = 0 \tag{3e}$$

$$\partial_t b_2 + \boldsymbol{v_2}\cdot\boldsymbol{\nabla} b_2 = 0 \tag{3f}$$

The **Equations (3a-f)** have to be applied in a defined domain $\mathbb{D}$ (latitudes x longitudes), and the boundary conditions begin with the specification of no normal flux condition $\hat{\boldsymbol{n}} \cdot h_i \boldsymbol{v}_i = 0$, with $x \in \partial\mathbb{D}$, and $\hat{\boldsymbol{n}}$ the outward unit vector.

The total energy of the system described by **Equations (3a-f)**, including both kinetic and gravitational potential components, is represented by the following Hamiltonian in **Equation (4a)**, and its functional derivatives in **(4b)**.

$$\mathcal{H} = \int_{\mathbb{D}} d^2x \left[h_1\left(\frac{1}{2}\boldsymbol{v}_1^2 + \tilde{h}_1 b_1\right) + h_2\left(\frac{1}{2}\boldsymbol{v}_2^2 + \tilde{h}_2 b_2\right)\right] \tag{4a}$$

https://doi.org/10.5194/egusphere-2026-512
Preprint. Discussion started: 30 April 2026

$$\frac{\delta \mathcal{H}}{\delta \boldsymbol{v}_k} = h_k \boldsymbol{v}_k, \qquad \frac{\delta \mathcal{H}}{\delta h_k} = \zeta_k, \qquad \frac{\delta \mathcal{H}}{\delta \boldsymbol{v}_k} = h_k \tilde{h}_k \tag{4b}$$

The concept of Bernoulli energy in each layer is represented by the expression $\zeta_i = \tilde{p}_i + (1/2)\boldsymbol{v}_i^2$. Here, k represents an elementary column part of the layer i. When calculating the Hamiltonian variation $\delta\mathcal{H}/\delta h_k$, the term $\partial \tilde{h}_k / \partial h_k$ generally does not vanish in the process. The free evolution of the system remains stable due to the conservation of its total mechanical energy, as specified in **Equation (4a)**. Under the Boussinesq approximation, the kinetic energy of an individual fluid column in each layer is given by $d^2x\ (1/2) h_i \boldsymbol{v}_i^2$. The absolute potential energy is then $d^2x\ h_i \overline{h}_i b_i$, where $\overline{h}_i$ is the height of each horizontal grid element of the layer (column above $z = 0$). This energy conservation holds for the combined kinetic and potential energy of the 2 layers, assuming a stably stratified configuration where $\theta_2 > \theta_1$ (for more details, see Ripa, 1993).

2.2 Buoyancy Anomaly Forcing

To investigate the dynamics of localized buoyancy disturbances, this study applies numerical simulations focusing on a large-scale positive buoyancy anomaly situated in the subtropical atmosphere. The analysis is carried out under two contrasting scenarios: one representing a dry (adiabatic environment) and the other incorporating moist-convective (MC) processes.

This experimental setup enables a focused examination of the fundamental mechanisms governing the evolution and dissipation of the buoyancy anomaly. With minimal external forcing, the results provide clearer insight into the core dynamical processes, improving the interpretability and robustness of the findings.

The initial buoyancy anomaly is introduced through a background buoyancy and wind velocity, plus a simplified formulation given in **Equation (5)**, expressed as a circular α-Gaussian distribution. Based on the approach of Rostami et al. (2023), the anomaly is spatially confined in both latitude and longitude, ensuring that its effects can be accurately tracked and analyzed throughout the simulation period. Including background effects in addition to the anomaly forcing is a new development relative to Rostami et al. (2023), enhancing the realism of the experiments.

$$b_i' = \varepsilon\, H_i \sqrt{2e}\, \frac{2^{\frac{1}{\sigma}}}{\sigma}\, \Gamma\left(\frac{1}{\sigma}+\frac{1}{2}\right) G\left(\frac{r^\sigma}{2}, \frac{1}{\sigma}+\frac{1}{2}\right), \quad H_1 = H_2 = 0.5 \tag{5}$$

The initial buoyancy anomaly is defined in non-dimensional form as b_i' (perturbation in layer i). This anomaly is controlled by two main parameters: ε, which sets the maximum amplitude, and σ, which controls its spatial extent or steepness. In our simulations, $\sigma = 4$. The radial distance r from the anomaly center to any given location is calculated using the Haversine formula $\mathbb{D}(Lat_0, Lon_0, Lat, Lon)$, where the center coordinates are $Lat_0 = 20°\ N$ and $Lon_0 = 40°\ W$, over the North Atlantic Ocean basin.

https://doi.org/10.5194/egusphere-2026-512
Preprint. Discussion started: 30 April 2026

To shape the spatial structure of the anomaly pattern, we utilize the function $G(r,a) = [1/\Gamma(a)] \int_r^a e^{-t}\, t^{a-1}\, dt$, where $\Gamma(x)$ is the Gamma function, and a is the Earth radius. Together, ε and σ determine both the magnitude and the radial decay of the buoyancy anomaly.

The model distinguishes between barotropic and baroclinic configurations. In the barotropic case, both atmospheric layers share the same buoyancy anomaly, such that $b_1' = b_2'$, resulting in vertically aligned disturbances with symmetric and horizontally expansive flow patterns. In contrast, the baroclinic configuration assumes a nonzero anomaly only in the lower layer ($b_1' > 0$, $b_2' = 0$), leading to vertical asymmetry and the development of cyclonic and anticyclonic structures due to the phase shift between layers. The configuration assumes stable stratification, characterized by $B_1 < B_2$, where B_1 and B_2 correspond to the background buoyancy fields in the state of rest.

To explore the influence of anomaly strength, we introduce two values for ε: 0.1, corresponding to a weak anomaly, and 0.2, representing a strong one. These variations allow us to assess the sensitivity of the atmospheric response under both moderate and intense perturbations.

In simulations involving moist convection, the initial specific humidity is prescribed to ensure strong vertical contrasts in moisture content. The lower layer is initialized close to saturation, while the upper layer remains far from saturation. This setup encourages condensation predominantly in the lower layer. Additionally, the model accounts for vertical entrainment of condensed liquid water content (CLWC) from the lower to the upper layer via convective updrafts (Rostami and Zeitlin, 2022).

To assess the potential dynamical impact of the imposed buoyancy disturbance, it is useful to consider its spatial scale. The anomaly, modeled as a circular α-Gaussian profile, spans about 32° in both the zonal and meridional directions at half its peak intensity. Notably, this scale aligns with the Rossby deformation radius typically observed in barotropic conditions at mid-latitudes. This alignment indicates that the disturbance is sufficiently large to interact with the background stratification and rotation in a dynamically meaningful way. Consequently, such a perturbation is capable of generating large-scale responses, including the excitation of Rossby waves and the onset of related atmospheric adjustments.

The model is initialized using monthly-averaged wind and potential temperature fields of June-1980 obtained from ERA5 reanalysis data (Hersbach et al., 2022). These initial conditions serve as the baseline for the simulation, allowing the system to evolve naturally under climatologically grounded dynamics. The localized thermal disturbance, presented here as the previous characterized circular buoyancy anomaly, is introduced after the model has freely evolved for five simulated model's days. This anomaly is imposed instantaneously in a single step and is not maintained throughout the integration, ensuring that the subsequent evolution reflects the system's intrinsic response rather than sustained external forcing. This approach allows for a clear isolation of the dynamical processes triggered by the anomaly within a subtropical latitude setting.

https://doi.org/10.5194/egusphere-2026-512
Preprint. Discussion started: 30 April 2026

3 Results

At the onset of the adjustment process triggered by the artificial imposed circular positive buoyancy anomaly at the initial steps, the system exhibits an almost uniform air movement flowing directed toward the anomaly's center in layer 1 (lower), and opposite in layer 2 (upper), varying only in intensity among the defined cases – weak and strong, in barotropic and baroclinic situations for a moist-convective environment – see **Fig. 2** and **3**. Similarly, simulations for a dry environment show almost the same behavior (**Supplementary Fig. S1-S2**).

This initial convergence pattern in layer 1 is driven by the formation of a localized low-pressure area that draws in surrounding air from all directions. As the system evolves, however, the influence of the Coriolis force (arising from the Earth's rotation) becomes increasingly significant. In the Northern Hemisphere, this force causes air to veer to the right, while in the Southern Hemisphere, it deflects to the left. Consequently, the wind field begins to shift away from purely radial inflow, giving rise to asymmetric convergence patterns. These directional imbalances lead to the formation of non-uniform structures in the divergence fields and the cloud liquid water content (CLWC), as depicted in **Fig. 4** and **5**. Additional zonal and meridional divergence temporal evolution are presented in **Supplementary Fig. S3-S6**.

The development of convergent zones around the buoyancy anomaly plays a central role in shaping moist-convective structures, particularly influencing the organization of precipitable water. These zones foster the emergence of distinct spiral rainband patterns encircling the anomaly, which arise from the dynamic interaction between inflowing air masses and the surrounding atmospheric environment (**Fig. 4** and **5, first row**, Layer 1). A key contributor to this behavior is the variation of the Coriolis parameter with latitude, which intensifies the system's asymmetry in a rotating spherical atmosphere.

Moreover, the asymmetric flow induced by the buoyancy anomaly introduces disturbances into the broader atmospheric circulation, potentially influencing nearby synoptic systems such as cyclones and anticyclones. The evolution of buoyancy anomalies and associated frontal systems in both lower and upper layers is primarily governed by geostrophic motions (where the pressure gradient and Coriolis forces are in balance) with additional modulation from ageostrophic effects, which stem from any imbalance between these forces.

The interaction between these circulations contributes to the formation and intensification of frontal boundaries, delineating air masses with contrasting thermal and density properties. This, in turn, promotes the development of precipitation characteristics and organized meteorological systems. Our analysis indicates that the presence of a strong buoyancy anomaly can act as a catalyst for triggering mesoscale convective systems, particularly in the vicinity west of the initially imposed disturbance for the weak case (**Fig. 4**, **last row**), and northeast in the strong case (**Fig. 5, last row**). These systems are capable of producing intense rainfall and are shaped by several factors, including the amplitude and scale of the anomaly, the vertical stratification of the atmosphere, wind shear, and the availability of environmental moisture.

https://doi.org/10.5194/egusphere-2026-512
Preprint. Discussion started: 30 April 2026

Our investigation shows that buoyancy anomalies in the lower troposphere can trigger the development of anticyclonic structures in the upper troposphere. More specifically, we find that such anticyclones may also form simultaneously as a result of positive potential temperature anomalies in lower levels. This supports the concept of simultaneous generation, in which cyclonic circulation appears near the surface while anticyclonic circulation develops aloft, creating more persistent and stable weather conditions that trap warm air masses (Sanders and Gyakum, 1980; Zaitchik et al., 2006; Fischer et al., 2007; White et al., 2023; Li et al., 2024). Consequently, in the later stages of our simulation, the main anticyclonic core shifts northward and gradually produces smaller secondary vortices, clearer in the simulations with initial strong buoyance imposition, in both baroclinic and barotropic cases (**Fig. 3**).

In similar simulations, although more simplified than those presented here, which did not include the effects of topography, Rostami et al. (2023) found comma-shaped patterns of precipitable water evolution in the upper troposphere, as also reported in other observational studies at mid-latitudes (e.g., Carlson, 1980; Carr and Millard, 1985; Reed and Blier, 1986ab; Businger and Hobbs, 1987). These patterns emerge during our simulations, most clearly around 30 days after initialization (**Fig. 3** and **5**, **timestep 1980-06-29**). This is related to the cyclonic flow in the lower troposphere and the anticyclonic flow in the upper troposphere (illustrated also by the zonal and meridional wind means in **Fig. 10**).

When subtropical latitude disturbances reach high amplitude, our simulations show that the geostrophic adjustment process excites inertia–gravity waves, which subsequently propagate equatorward and dissipate in the tropics, playing an important role in redistributing heat and momentum in the lower troposphere. As the atmosphere begins to adjust in our simulations, it quickly responds by releasing a burst of inertia-gravity waves, as shown in more details in baroclinic arranged results for strong buoyance anomaly case (**last row** in **Fig. 3**). These early-stage waves are clearly visible in the wave activity diagrams (**Figure 8**), where we track them by integrating the divergence of the velocity field. The zonal mean of divergence brings the latitudinal aspect for the inertia-gravity waves, remarking for all simulations the particularity of higher values toward the south of the imposed anomaly (**Fig. 9**). That is because the added moisture and ascending motion in these regions trigger more intense condensation, related to the model layer thicknesses (h_i) and buoyancy variables (b_i; **Equations (1a-h)**), which in turn favors stronger wave generation in those southern areas.

The comparison between baroclinic and barotropic configurations in the MC and Dry experiments shows that inertia-gravity wave activity (**Fig. 8**) initially responds intensely in layers 1 and 2, due to the extreme anomaly imposed. This forcing generates temperature gradients between the atmospheric layers, resulting in the formation of the cyclones and anticyclones previously discussed. As the simulations progress, however, wave activity tends to decline over the two months analyzed, toward an equilibrium. In particular, the baroclinic case with the strong initial anomaly in MC environment performed the highest peak of wave activity than in the other experiments, which means the model's vertical scheme can respond correctly to those different temperature gradient extremes scenarios. The analogous baroclinic configuration for the dry environment does not simulate an equal aspect of the peak in lower layer, that can be related to the differences in convective formation, where the

https://doi.org/10.5194/egusphere-2026-512
Preprint. Discussion started: 30 April 2026

MC case is able to release more energy to the upper layer by the entrainment. In the upper layer, the behaviors of the MC and Dry configuration pairs are very close until the end of the integration, with the greatest differences associated with the intensity of the initial anomaly: the strong cases shows higher wave activity compared to the weak cases.

The evolution of buoyancy anomalies is strongly influenced by their interaction with Rossby waves and beta gyres. At the initial stage, the slower westward phase speed of Rossby waves at higher latitudes causes perturbations at lower latitudes to advance in phase, producing a northeast-southwest tilt in the buoyancy field (**Fig. 2** and **3**). As the system evolves, the anomalies develop a comma-shaped structure and are advected northward by beta gyres. The strength and trajectory of these anomalies depend on factors such as the disturbance amplitude, the presence of moist convection, and whether the vertical structure is barotropic or baroclinic. The asymmetry generated by the beta gyres enhances system instability, leading to core fragmentation and the formation of secondary mesovortices (**Fig. 2** and **3**), a feature also documented in tropical cyclones (e.g., Fang and Zhang, 2012; Schecter, 2018). More intense anomalies tend to exhibit stronger meridional displacements, first drifting northwestward and later turning eastward, a behavior particularly pronounced in barotropic configurations.

Overall, the effects of these anomalies manifest in opposite ways when comparing total energy fluxes with tropospheric water content variables. **Fig. 6** and **7** illustrate that the integrated evolution of CLWC, the Bulk of precipitable water (W2), and the Hamiltonian exhibits a relatively inverse relationship. Specifically, positive buoyancy anomalies can trigger heatwaves and atmospheric instability, enhancing moist convection across model layers and promoting the development of rainbands in certain regions (**Fig. 4** and **5**), while producing opposite effects in others, depending on the experiment configurations. This process is sustained by a positive feedback cycle, in which latent heat release further intensifies convection. Thus, the atmospheric adjustment continues until the disturbance dissipates, restoring stability.

https://doi.org/10.5194/egusphere-2026-512
Preprint. Discussion started: 30 April 2026

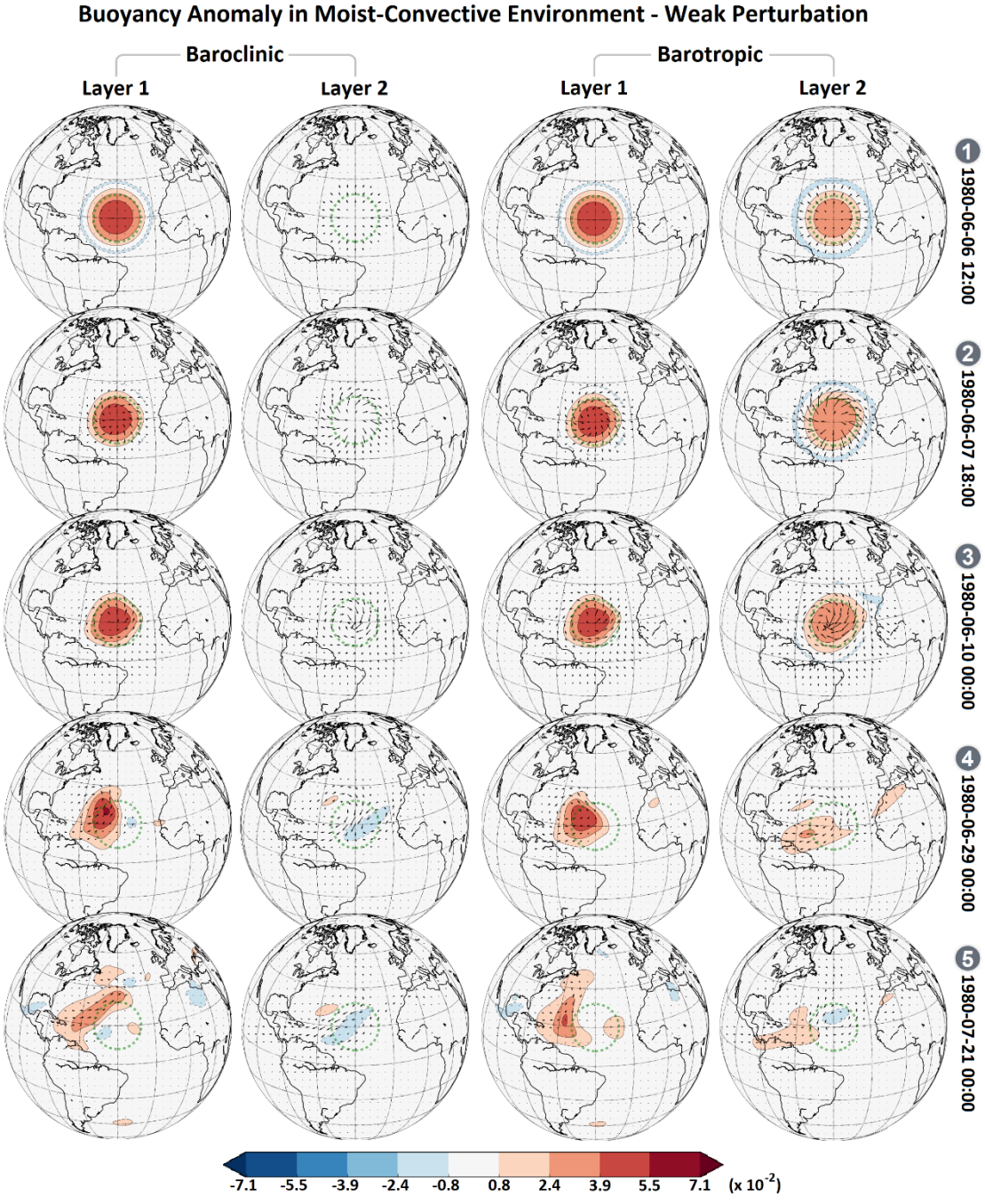

Figure 2: Anomaly evolution of buoyancy by weak perturbation, in the lower (Layer 1) and upper (Layer 2) troposphere, and the corresponding velocity field (represented by arrows) during adjustment in a moist-convective environment, in respect to the reference case. The first and second columns show the results for baroclinic configuration and the third and fourth columns for barotropic. ERA5 monthly-averaged data was used as initial condition to startup the model from 1-June-1980.

https://doi.org/10.5194/egusphere-2026-512
Preprint. Discussion started: 30 April 2026

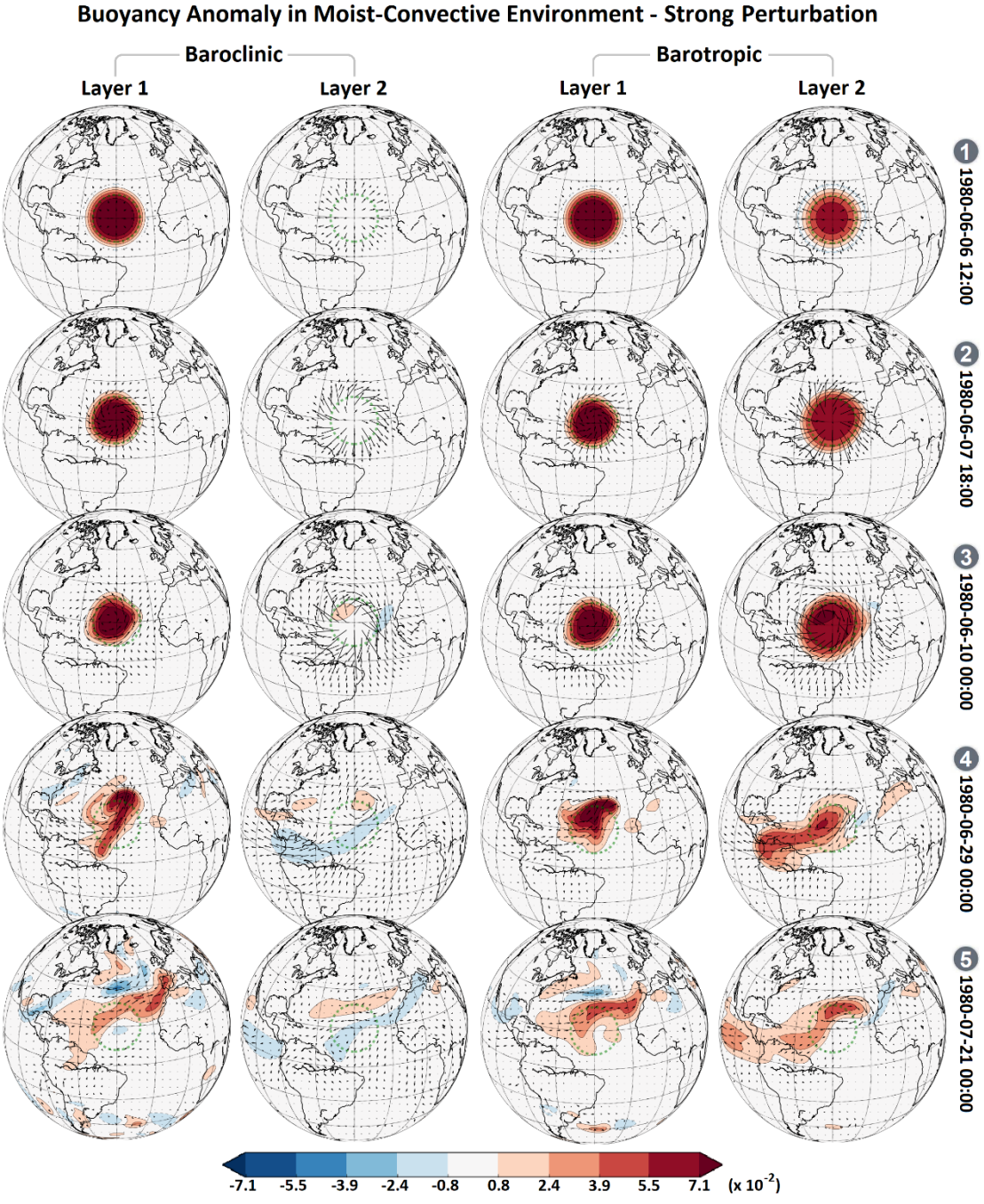

Figure 3: Anomaly evolution of buoyancy by strong perturbation, in the lower (Layer 1) and upper (Layer 2) troposphere, and the corresponding velocity field (represented by arrows) during adjustment in a moist-convective environment, in respect to the reference case. The first and second columns show the results for baroclinic configuration and the third and fourth columns for barotropic. ERA5 monthly-averaged data was used as initial condition to startup the model from 1-June-1980.

https://doi.org/10.5194/egusphere-2026-512
Preprint. Discussion started: 30 April 2026

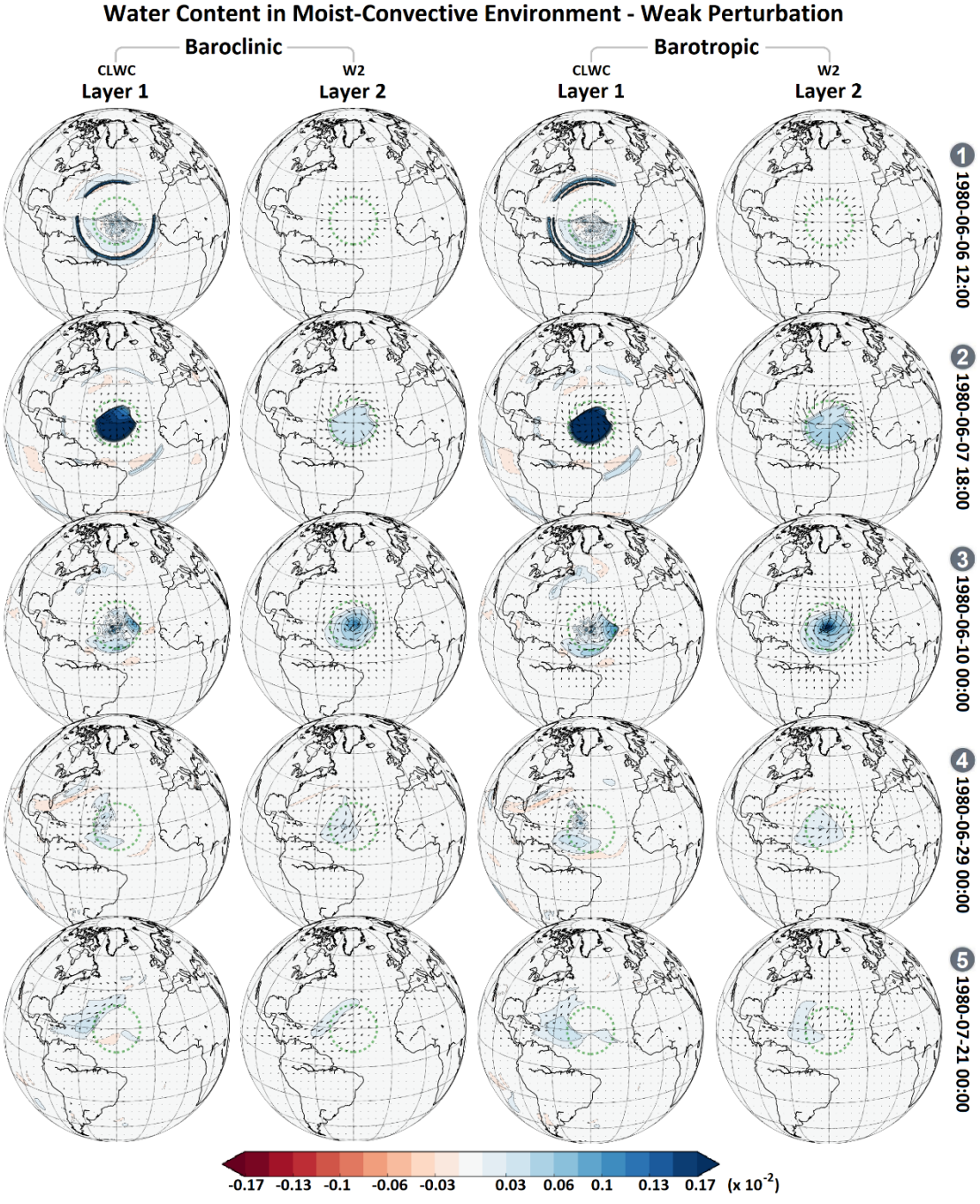

Figure 4: Anomaly evolution of CLWC (Condensed liquid water content) by weak perturbation in the lower troposphere (Layer 1), and W2 (Bulk of precipitable water) in the upper troposphere (Layer 2), and the corresponding velocity field (represented by arrows) during adjustment in a moist-convective environment, in respect to the reference case. The first and second columns show the results for baroclinic configuration and the third and fourth columns for barotropic.

https://doi.org/10.5194/egusphere-2026-512
Preprint. Discussion started: 30 April 2026

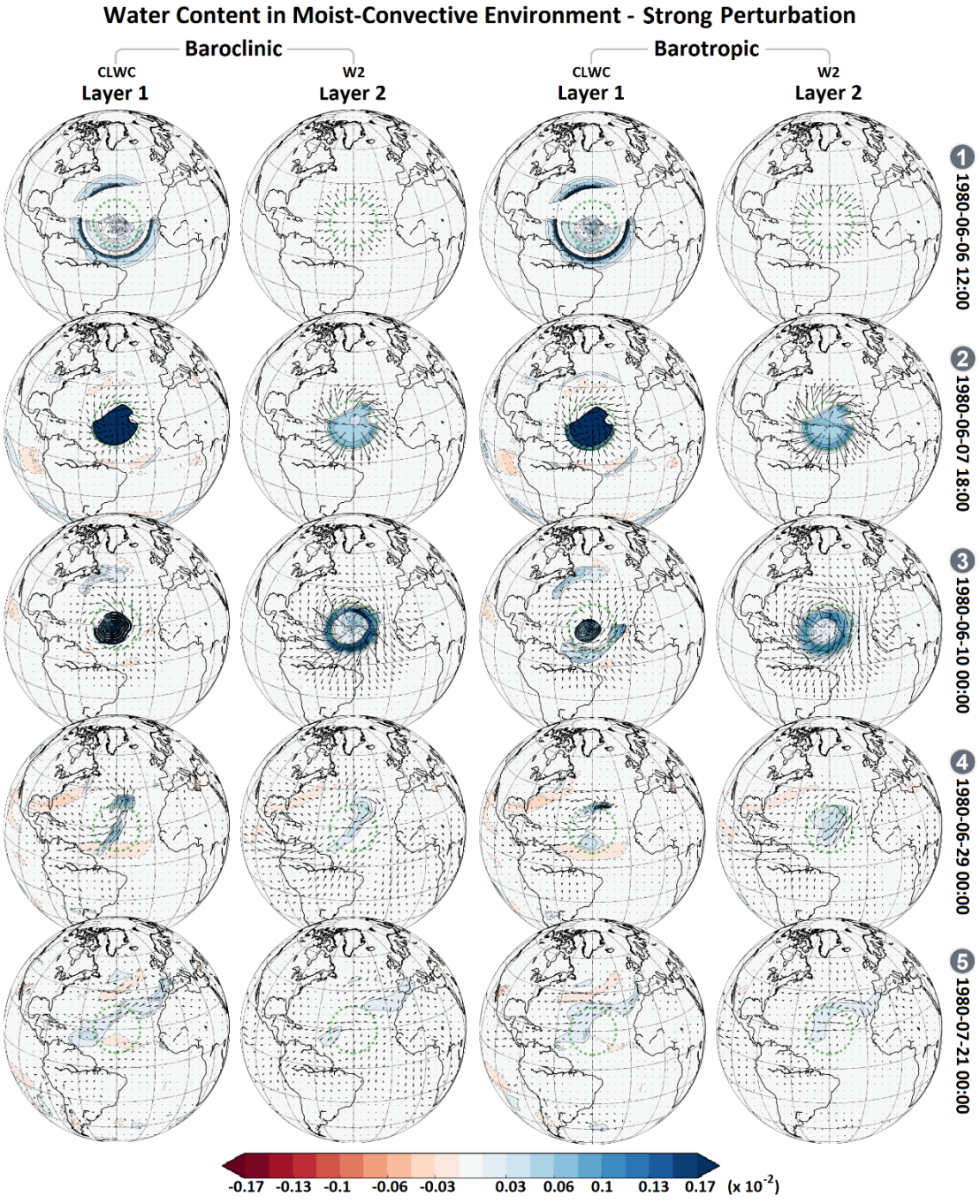

Figure 5: Anomaly evolution of CLWC (Condensed liquid water content) by strong perturbation in the lower troposphere (Layer 1), and W2 (Bulk of precipitable water) in the upper troposphere (Layer 2), and the corresponding velocity field (represented by arrows) during adjustment in a moist-convective environment, in respect to the reference case. The first and second columns show the results for baroclinic configuration and the third and fourth columns for barotropic.

https://doi.org/10.5194/egusphere-2026-512
Preprint. Discussion started: 30 April 2026

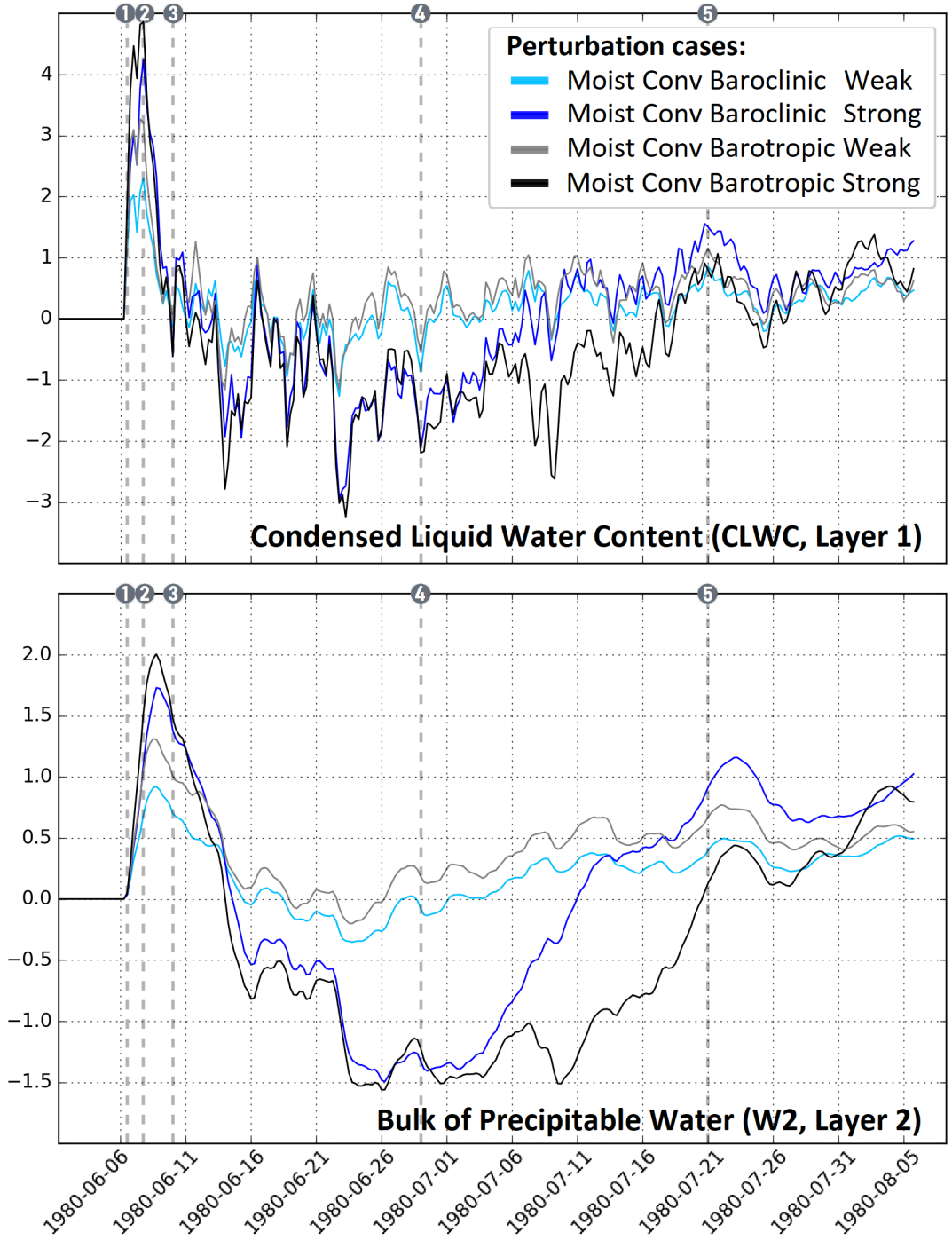

Figure 6: Global anomaly of CLWC and W2 relative to the reference case. Markers on the top border indicate the time-steps of maps displayed in previous figures.

https://doi.org/10.5194/egusphere-2026-512
Preprint. Discussion started: 30 April 2026

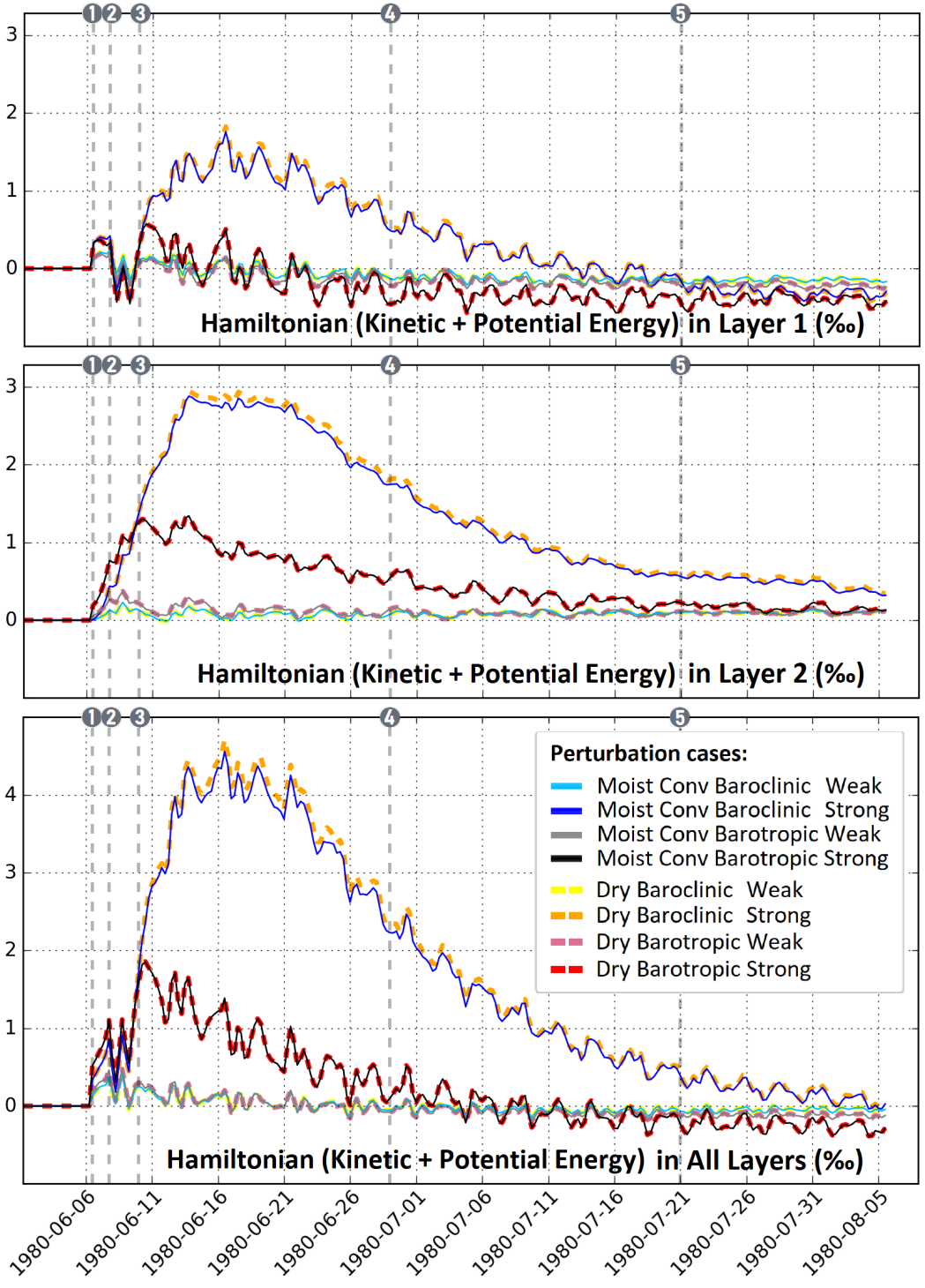

320 **Figure 7**: Global mean anomaly of Hamiltonian relative to the reference case, calculated by $(\mathcal{H} - \mathcal{H}_{t=0})1000/\mathcal{H}_{t=0}$. Markers on the top border indicate the time-steps of maps displayed in previous figures.

https://doi.org/10.5194/egusphere-2026-512
Preprint. Discussion started: 30 April 2026

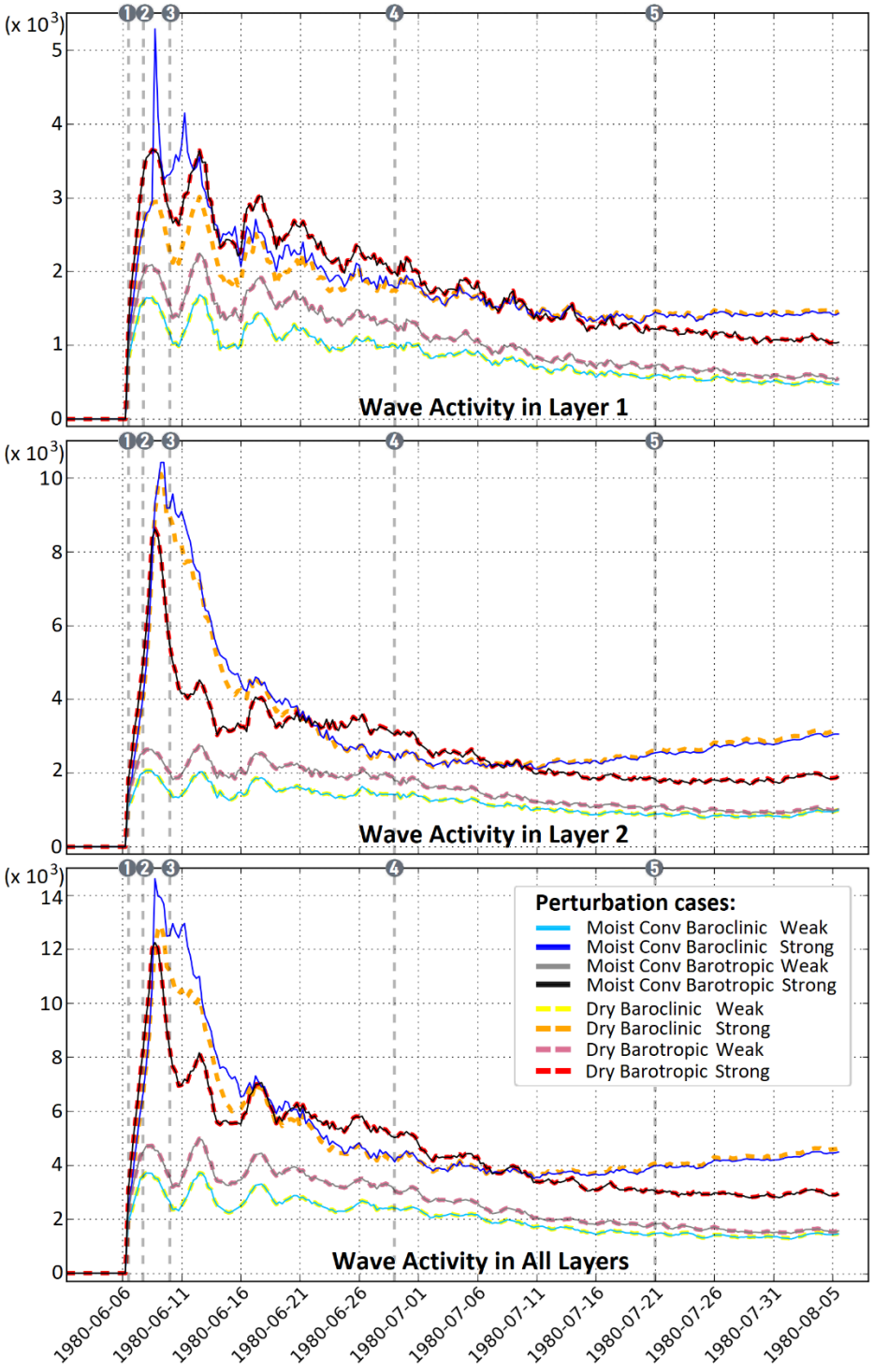

Figure 8: Global anomaly of Wave Activity relative to the reference case. Markers on the top border indicate the time-steps of maps displayed in previous figures.

https://doi.org/10.5194/egusphere-2026-512
Preprint. Discussion started: 30 April 2026

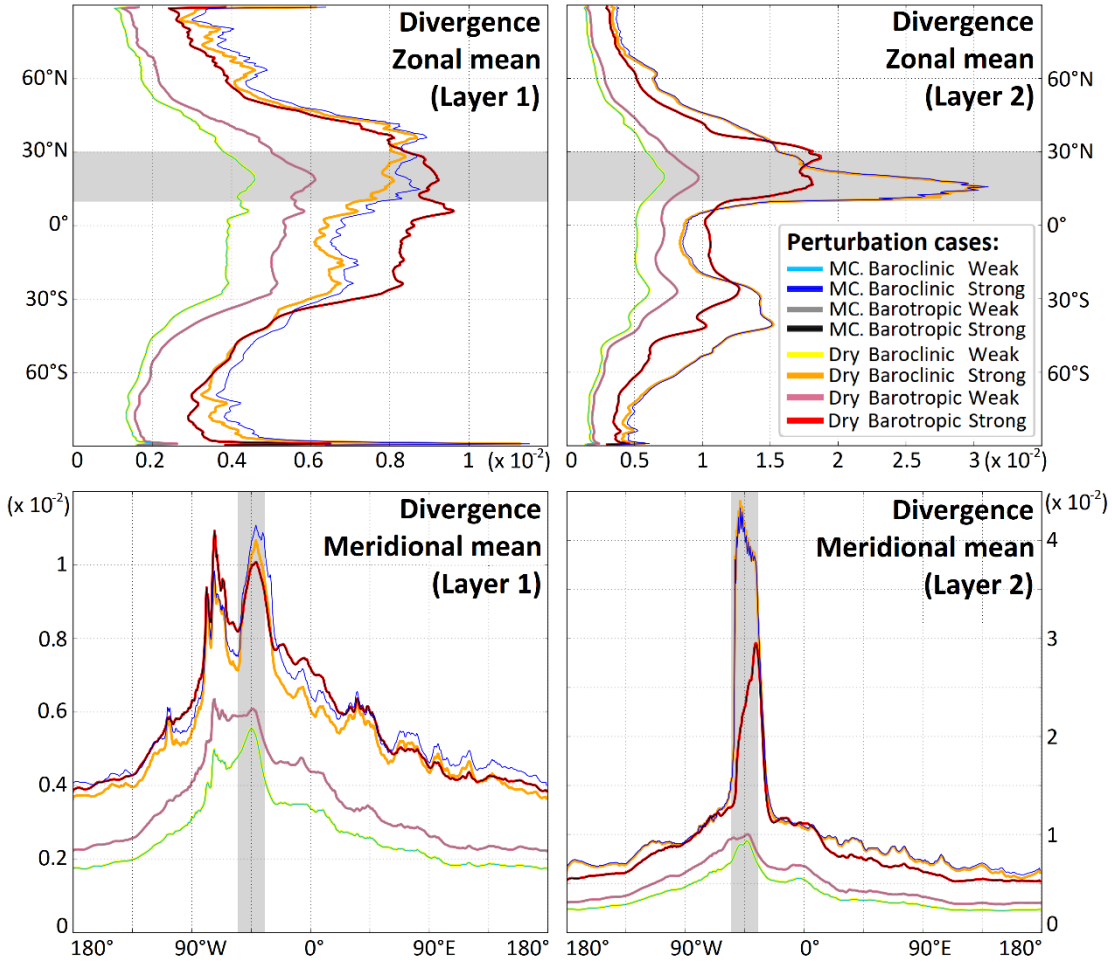

Figure 9: Divergence anomaly time-mean (1-June to 5-Aug 1980) relative to the reference case, for moist-convective (MC) and dry situations. The gray shade represents the initial buoyancy perturbation region.

https://doi.org/10.5194/egusphere-2026-512
Preprint. Discussion started: 30 April 2026

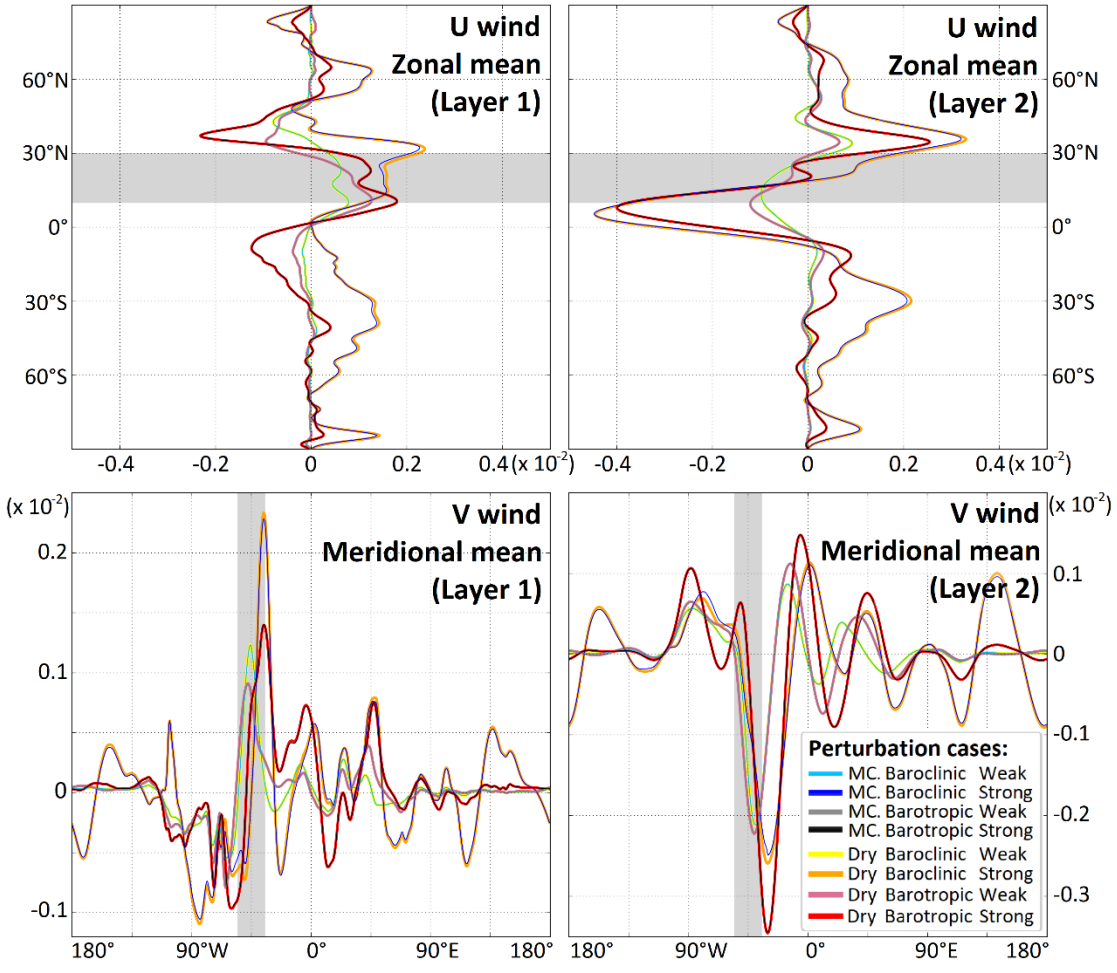

Figure 10: Wind anomaly time-mean (1-June to 5-Aug 1980) relative to the reference case, for moist-convective (MC) and dry situations. The gray shade represents the initial buoyancy perturbation region.

https://doi.org/10.5194/egusphere-2026-512
Preprint. Discussion started: 30 April 2026

4 Conclusions

This study set out to explore the dynamics of localized extreme heatwaves in the subtropical atmosphere through an intermediate complexity modeling approach using Aeolus 2.0. By imposing buoyancy anomalies under both dry and moist-convective conditions, we were able to disentangle the primary processes that govern the emergence, development, and eventual dissipation of these extreme events. The results provide a coherent picture of how localized heating triggers large-scale atmospheric responses that can persist for extended periods.

A central finding is the role of the imposed buoyancy anomaly in shaping the initial adjustment process simulated by the multi-layer formulation of the moist-convective Thermal Rotating Shallow Water (mcTRSW) model framework.

Early in the simulations, convergence in the lower troposphere and divergence in the upper troposphere set the stage for cyclonic and anticyclonic circulation patterns. These patterns quickly departed from radial symmetry as the Coriolis force came into play, highlighting the sensitivity of heatwave development to planetary rotation and latitudinal gradients.

The simulations further demonstrated the emergence of spiral rainband-like structures encircling the buoyancy anomaly. These mesoscale features, particularly evident in moist-convective scenarios, emphasize the importance of moisture feedbacks in strengthening instability. Latent heat release during condensation amplified convection, generating a positive feedback loop that sustained rainfall bands and reinforced the heatwave environment.

Inertia–gravity waves were found to be an integral part of the atmospheric response. Triggered during the early adjustment, these waves propagated equatorward and contributed to the redistribution of heat and momentum. Their presence was strongest in baroclinic configurations with intense initial anomalies, and their decay over time marked the transition toward equilibrium. The sensitivity of wave activity to environmental moisture underlines the value of including moist-convective processes in idealized frameworks.

Another key outcome of this study is the simultaneous generation of cyclonic and anticyclonic structures. Lower-level positive buoyancy anomalies induced cyclonic circulations near the surface, while anticyclones emerged aloft. This vertical coupling, consistent with the simultaneous generation paradigm, promoted stable atmospheric ridges that trapped warm air masses. The northward drift and eventual fragmentation of the anticyclonic core into smaller vortices further reflect the dynamical richness of these systems.

The simulations also reproduced comma-shaped patterns in precipitable water, a well-known observational feature of subtropical cyclones. These structures emerged roughly one month into the integrations, driven by the interplay of lower-tropospheric cyclonic flow and upper-tropospheric anticyclonic circulation. Their occurrence in both moist and dry environments underscores the robustness of this dynamical signature.

https://doi.org/10.5194/egusphere-2026-512
Preprint. Discussion started: 30 April 2026

Comparisons between baroclinic and barotropic settings revealed systematic differences. Baroclinic experiments, especially under moist-convective forcing, exhibited stronger inertia–gravity wave activity and greater sensitivity to the amplitude of the initial buoyancy anomaly. In contrast, barotropic environments showed more pronounced meridional shifts of buoyancy anomalies and a stronger tendency for eastward drift at later stages. These distinctions demonstrate how vertical structure can influence the path along which heat waves evolve.

Rossby wave dynamics and beta gyres also emerged as fundamental mechanisms. Phase speed differences across latitudes tilted the buoyancy anomalies in a northeast–southwest orientation, later advected poleward by beta gyres. The asymmetries induced by these gyres amplified system instability, fragmenting the core circulation and giving rise to secondary mesovortices. Such processes link idealized simulations to real-world observations of instability and breakdown in subtropical and mid-latitude weather systems.

Energy and moisture diagnostics further highlighted the dual nature of buoyancy anomalies. The integrated evolution of the Hamiltonian energy fluxes and tropospheric water variables revealed an inverse relationship. While positive buoyancy anomalies strengthened instability and rainfall formation in some regions, they simultaneously suppressed moist processes elsewhere. This spatial heterogeneity emphasizes the non-linear and regionally dependent character of heatwave evolution.

Taken together, these findings indicate that localized surface heating can initiate complex chains of atmospheric adjustment that resonate from the mesoscale to the synoptic scale. The interplay of inertia–gravity waves, Rossby wave dynamics, convective feedbacks, and vertical structural differences creates a multifaceted environment where heatwaves can persist, intensify, and interact with larger-scale circulation patterns.

Compared to studies based on earlier versions of our model, adding certain real-world characteristics, such as topography and background wind velocity effects, in a novel development that improves the fidelity of the experiments, the model simulates the essential dynamics of buoyancy-driven anomalies. The success in reproducing phenomena observed in nature like rainbands, comma-cloud patterns, ridged trough coupling validates the approach and provides a bridge between theory and fully comprehensive climate simulations.

In conclusion, our results shed new light on the fundamental processes underlying subtropical heatwaves. They underscore the importance of buoyancy anomalies as drivers of multi-scale atmospheric responses, highlight the necessity of accounting for moist convection, and reaffirm the coupling between cyclonic and anticyclonic circulations. These insights contribute to the ongoing effort to build a more complete theoretical framework for heatwave dynamics, ultimately improving our ability to anticipate, model, and respond to extreme events in a changing climate.

https://doi.org/10.5194/egusphere-2026-512
Preprint. Discussion started: 30 April 2026

Supplementary Materials

Supplementary material for this article is available at:

<Link to the Supplementary material document submitted with this article>

Acknowledgments

The authors gratefully acknowledge the Ministry of Research, Science and Culture (MWFK) of Land Brandenburg for supporting this project by providing resources on the high performance computer system at the Potsdam Institute for Climate Impact Research (Grant No. 22-Z105-05/002/001).

This work was supported by the Potsdam Institute for Climate Impact Research (PIK) under Project Atmo-POEM funded by H&M Foundation. The University of Potsdam contributed to the work by the first author's association as a Ph.D. candidate.

Conflict of Interest

The authors have no conflicts to disclose.

Author Contributions

Sullyandro Guimarães: Conceptualization; Methodology; Modelling; Software; Visualization; Formal analysis; Investigation; Validation; Writing – original draft; Writing – review & editing.

Masoud Rostami: Conceptualization; Methodology; Modelling; Software; Visualization; Formal analysis; Investigation; Validation; Writing – review & editing.

Stefan Petri: Modelling; Software; Investigation; Validation; Writing – review & editing.

All authors discussed the results, edited and reviewed the manuscript.

Code and data availability

The code and data that support the findings of this study are openly available in Zenodo at Guimarães et al. (2025; v2, https://doi.org/10.5281/zenodo.18065000), reference number 18065000.

The Aeolus 2.0 code included in the above-mentioned repository was adapted with small changes from Rostami et al. (2024b; v6, https://doi.org/10.5281/zenodo.13768553).

https://doi.org/10.5194/egusphere-2026-512
Preprint. Discussion started: 30 April 2026

References

Barriopedro, D., García-Herrera, R., Ordóñez, C., Miralles, D. G., Salcedo-Sanz, S. Heat waves: Physical understanding and scientific challenges. *Reviews of Geophysics*, **61**, e2022RG000780. DOI: 10.1029/2022RG000780, 2023.

Betts, A., Miller, M. A new convective adjustment scheme. Part II: Single columns tests using GATE wave, BOMEX, ATEX and arctic air-mass data sets. *Quarterly Journal of the Royal Meteorological Society*, **112**, 693-762. DOI: 10.1002/qj.49711247308, 1986.

Bouchut, F., Lambaerts, J., Lapeyre, G., Zeitlin, V. Fronts and nonlinear waves in a simplified shallow-water model of the atmosphere with moisture and convection. *Physics of Fluids*, **21**, 116604. DOI: 10.1063/1.3265970, 2009.

Burns, K. J., Vasil, G. M., Oishi, J. S., Lecoanet, D., Brown, B. P. Dedalus: A Flexible Framework for Numerical Simulations with Spectral Methods. *Physical Review Research*, **2** (2). DOI: 10.1103/PhysRevResearch.2.023068, 2020.

Businger, S., Hobbs, P. V. Mesoscale Structures of Two Comma Cloud Systems over the Pacific Ocean. *Monthly Weather Review*, **115** (9), 1908-1928. DOI: 10.1175/1520-0493(1987)115<1908:MSOTCC>2.0.CO;2, 1987.

Cao, Y., Kurganov, A., Liu, Y., Rostami, M., Zeitlin, V. On the dynamics of equatorial excited dipolar systems. *Physics of Fluids*, **37** (5), 056618. DOI: 10.1063/5.0270628, 2025.

Carlson, T. N. Airflow through midlatitude cyclones and the comma cloud pattern. *Monthly Weather Review*, **108**, 1498-1509. DOI: 10.1175/1520-0493(1980)108<1498:ATMCAT>2.0.CO;2, 1980.

Carr, F. H., Millard, J. P. A Composite Study of Comma Clouds and their Association with Severe Weather over the Great Plains. *Monthly Weather Review*, **113** (3), 370-387. DOI: 10.1175/1520-0493(1985)113<0370:ACSOCC>2.0.CO;2, 1985.

Fang, J., Zhang, F. Effect of Beta Shear on Simulated Tropical Cyclones. *Monthly Weather Review*, **140** (10), 3327-3346. DOI: 10.1175/MWR-D-10-05021.1, 2012.

Fischer, E. M., Seneviratne, S. I., Vidale, P. L., Lüthi, D., Schär, C. Soil moisture-atmosphere interactions during the 2003 European summer heat wave. *Journal of Climate*, **20**, 5081-5099. DOI: 10.1175/JCLI4288.1, 2007.

Gao, Y., Wu, Y., Guo, X., Kou, W., Zhang, S., Leung, L. R., et al. More frequent and persistent heatwaves due to increased temperature skewness projected by a high-resolution Earth System Model. *Geophysical Research Letters*, **50**, e2023GL105840. DOI: 10.1029/2023GL105840, 2023.

https://doi.org/10.5194/egusphere-2026-512
Preprint. Discussion started: 30 April 2026

Gill, A. Studies of moisture effects in simple atmospheric models: The stable case. *Geophysical & Astrophysical Fluid Dynamics*, **19**, 119. DOI: 10.1080/03091928208208950, 1982.

Guimarães, S. O., Mann, M. E., Rahmstorf, S., Petri, S., Steinman, B. A., Brouillette, D. J., Christiansen, S., Li, X. Increased projected changes in quasi-resonant amplification and persistent summer weather extremes in the latest multimodel climate projections. *Scientific Reports*, **14**, 21991. DOI: 10.1038/s41598-024-72787-0, 2024.

Guimarães, S. O., Rostami, M., Petri, S. Materials for the Article "Subtropical Extreme Heatwave Dynamics in the Intermediate-Complexity Atmospheric Model Aeolus 2.0". *Zenodo*, **v2**. DOI: 10.5281/zenodo.18065000, 2025.

Hao, Z., Hao, F., Xia, Y., Feng, S., Sun, C., Zhang, X., Fu, Y., Hao, Y., Zhang, Y., Meng, Y. Compound droughts and hot extremes: Characteristics, drivers, changes, and impacts. *Earth-Science Reviews*, **235**, 104241. DOI: 10.1016/j.earscirev.2022.104241, 2022.

Hersbach, H., Bell, B., Berrisford, P., et al. The ERA5 global reanalysis. *Quarterly Journal of the Royal Meteorological Society*, **146**, 1999–2049. DOI: 10.1002/qj.3803, 2020.

Holton, J. R., Hakim, G. J. An Introduction to Dynamic Meteorology. *Elsevier*, Book Fifth Edition. DOI: 10.1016/C2009-0-63394-8, 2013.

Hoskins, B. J., Karoly, D. J. The Steady Linear Response of a Spherical Atmosphere to Thermal and Orographic Forcing. *Journal of Atmospheric Sciences*, **38** (6), 1179-1196. DOI: 10.1175/1520-0469(1981)038<1179:TSLROA>2.0.CO;2, 1981.

Kautz, L. -A., Martius, O., Pfahl, S., Pinto, J. G., Ramos, A. M., Sousa, P. M., Woollings, T. Atmospheric blocking and weather extremes over the Euro-Atlantic sector – a review. *Weather and Climate Dynamics*, **3**, 305–336. DOI: 10.5194/wcd-3-305-2022, 2022.

Kurganov, A., Liu, Y., Zeitlin, V. Moist-convective thermal rotating shallow water model. *Physics of Fluids*, **32** (6), 066601. DOI: 10.1063/5.0007757, 2020.

Lambaerts, J., Lapeyre, G., Zeitlin, V. Moist versus dry barotropic instability in a shallow-water model of the atmosphere with moist convection. *Journal of the Atmospheric Sciences*, **68**, 1234-1252. DOI: 10.1175/2011JAS3540.1, 2011a.

Lambaerts, J., Lapeyre, G., Zeitlin, V., Bouchut, F. Simplified two-layer models of precipitating atmosphere and their properties. *Physics of Fluids*, **23**, 046603. DOI: 10.1063/1.3582356, 2011b.

https://doi.org/10.5194/egusphere-2026-512
Preprint. Discussion started: 30 April 2026

Lambaerts, J., Lapeyre, G., Zeitlin, V. Moist versus dry baroclinic instability in a simplified two-layer atmospheric model with condensation and latent heat release. *Journal of the Atmospheric Sciences*, **69**, 1405-1426. DOI: 10.1175/JAS-D-11-0205.1, 2012.

Lecoanet, D., Vasil, G. M., Burns, K. J., Brown, B. P., Oishi, J. S. Tensor calculus in spherical coordinates using Jacobi polynomials. Part-II: Implementation and Examples. *Journal of Computational Physics*, **3**, 100012. DOI: 10.1016/j.jcpx.2019.100012, 2019.

Li, X., M. Mann, M. E., Wehner, F., Rahmstorf, S., Petri, S., Christiansen, S., Carrillo, J. Role of atmospheric resonance and land–atmosphere feedbacks as a precursor to the June 2021 Pacific Northwest Heat Dome event. *Proceedings of the National Academy of Sciences of the United States of America*, **121** (4), e2315330121. DOI: 10.1073/pnas.2315330121, 2024.

Liu, Z., Wang, L. Blocking diversity causes distinct roles of diabatic heating in the Northern Hemisphere. *Nature communications*, **16** (1), 5613. DOI: 10.1038/s41467-025-60811-4, 2025.

Miralles, D. G., Gentine, P., Seneviratne, S. I., Teuling, A. J. Land-atmospheric feedbacks during droughts and heatwaves: state of the science and current challenges. *Annals of the New York Academy of Sciences*, **1436**, 19-35. DOI: 10.1111/nyas.13912, 2019.

Nabizadeh, E., Lubis, S. W., Hassanzadeh, P. The 3D Structure of Northern Hemisphere Blocking Events: Climatology, Role of Moisture, and Response to Climate Change. *Journal of Climate*, **34**, 9837–9860. DOI: 10.1175/JCLI-D-21-0141.1, 2021.

Petoukhov, V., Rahmstorf, S., Petri, S., Schellnhuber, H. J. Quasiresonant amplification of planetary waves and recent Northern Hemisphere weather extremes. *Proceedings of the National Academy of Sciences of the United States of America*, **110** (14), 5336–5341. DOI: 10.1073/pnas.1222000110, 2013.

Pfahl, S., Wernli, H. Quantifying the relevance of atmospheric blocking for co-located temperature extremes in the Northern Hemisphere on (sub-)daily time scales. *Geophysical Research Letters*, **39**. DOI: 10.1029/2012GL052261, 2012.

Reed, R. J., Blier, W. A Case Study of Comma Cloud Development in the Eastern Pacific. *Monthly Weather Review*, **114** (9), 1681-1695. DOI: 10.1175/1520-0493(1986)114<1681:ACSOCC>2.0.CO;2, 1986a.

Reed, R. J., Blier, W. A Further Study of Comma Cloud Development in the Eastern Pacific. *Monthly Weather Review*, **114** (9), 1696-1708. DOI: 10.1175/1520-0493(1986)114<1696:AFSOCC>2.0.CO;2, 1986b.

Ripa, P. Conservation laws for primitive equations models with inhomogeneous layers. *Geophysical & Astrophysical Fluid Dynamics*, **70**, 85-111. DOI: 10.1080/03091929308203588, 1993.

https://doi.org/10.5194/egusphere-2026-512
Preprint. Discussion started: 30 April 2026

Rostami, M., Zeitlin, V. An improved moist-convective rotating shallow-water model and its application to instabilities of hurricane like vortices. *Quarterly Journal of the Royal Meteorological Society*, **144**, 1450-1462. DOI: 10.1002/qj.3292, 2018.

Rostami, M., Zeitlin, V. Instabilities of low-latitude easterly jets in the presence of moist convection and topography and related cyclogenesis, in a simple atmospheric model. *Geophysical & Astrophysical Fluid Dynamics*, **116**, 56-77. DOI: 10.1080/03091929.2021.1959574, 2022.

Rostami, M., Zhao, B., Petri, S. On the genesis and dynamics of Madden-Julian oscillation-like structure formed by equatorial adjustment of localized heating. *Quarterly Journal of the Royal Meteorological Society*, **148** (749), 3788-3813. DOI: 10.1002/qj.4388, 2022.

Rostami, M., Severino, L., Petri, S., Hariri, S. Dynamics of localized extreme heatwaves in the mid-latitude atmosphere: A conceptual examination. *Atmospheric Science Letters*, **25** (1), e1188. DOI: 10.1002/asl.1188, 2023.

Rostami, M., Petri, S., Guimarães, S. O., Fallah, B. Open-source stand-alone version of atmosphere model Aeolus 2.0 Software. *Geoscience Data Journal*, **11**, 1086–1093. DOI: 10.1002/gdj3.249, 2024a.

Rostami, M., Petri, S., Guimarães, S. O., Fallah, B. Open-source stand-alone version of atmosphere model Aeolus 2.0 Software. *Zenodo*, **v6**. DOI: 10.5281/zenodo.13768553, 2024b.

Rostami, M., Petri, S., Fallah, B., Fazel-Rastgar, F. Aeolus 2.0's thermal rotating shallow water model: A new paradigm for simulating extreme heatwaves, westerly jet intensification, and more. *Physics of Fluids*, **37** (1), 016604. DOI: 10.1063/5.0244908, 2025a.

Rostami, M., Petri, S., Fallah, B., Fazel-Rastgar, F. A novel sea surface evaporation scheme assessed by the thermal rotating shallow water model. *Atmospheric Science Letters*, **26** (1), e1287. DOI: 10.1002/asl.1287, 2025b.

Rouges, E., Ferranti, L., Kantz, H., Pappenberger, F. European heatwaves: Link to large-scale circulation patterns and intraseasonal drivers. *International Journal of Climatology*, **43** (7), 3189–3209. DOI: 10.1002/joc.8024, 2023.

Sanders, F., Gyakum, J. R. Synoptic-Dynamic Climatology of the “Bomb”. *Monthly Weather Review*, **108**, 1589-1606. DOI: 10.1175/1520-0493(1980)108<1589:SDCOT>2.0.CO;2, 1980.

Schaller, N., Sillmann, J., Anstey, J., et al. Influence of blocking on Northern European and Western Russian heatwaves in large climate model ensembles. *Environmental Research Letters*, **13**, 5, 054015. DOI: 10.1088/1748-9326/aaba55, 2018.

https://doi.org/10.5194/egusphere-2026-512
Preprint. Discussion started: 30 April 2026

Schecter, D. A. On the instabilities of tropical cyclones generated by cloud resolving models. *Tellus A: Dynamic Meteorology and Oceanography*, **70** (1), 1–30. DOI: 10.1080/16000870.2018.1525245, 2018.

Schemm, S., Rüdisühli, S., Sprenger, M. The life cycle of upper-level troughs and ridges: a novel detection method, climatologies and Lagrangian characteristics. *Weather and Climate Dynamics*, **1**, 459–479. DOI: 10.5194/wcd-1-459-2020, 2020.

Sousa, P. M., Barriopedro, D., García-Herrera, R., Woollings, T., Trigo, R. M. A New Combined Detection Algorithm for Blocking and Subtropical Ridges. *Journal of Climate*, **34** (18), 7735-7758. DOI: 10.1175/JCLI-D-20-0658.1, 2021.

Vasil, G. M., Lecoanet, D., Burns, K. J., Oishi, J. S., Brown, B. P. Tensor calculus in spherical coordinates using Jacobi polynomials. Part-I: Mathematical analysis and derivations. *Journal of Computational Physics*, **3**, 100013. DOI: 10.1016/j.jcpx.2019.100013, 2019.

Wang, M., Huang, Y., Franzke, C. L. E., et al. Evidence for preferred propagating terrestrial heatwave pathways due to Rossby wave activity. *Nature Communications*, **16**, 4742. DOI: 10.1038/s41467-025-60104-w, 2025.

White, R. H., Anderson, S., Booth, J. F., Braich, G., Draeger, C., Fei, C., Harley, C. D. G., Henderson, S. B., Jakob, M., Lau, C. -A., Mareshet Admasu, L., Narinesingh, V., Rodell, C., Roocroft, E., Weinberger, K. R, West, G. The unprecedented Pacific Northwest heatwave of June 2021. *Nature Communications*, **14**, 727. DOI: 10.1038/s41467-023-36289-3, 2023.

Zaitchik, B. F., Macalady, A. K., Bonneau, L. R., Smith, R. B. Europe's 2003 heat wave: a satellite view of impacts and land-atmosphere feedbacks. *International Journal of Climatology*, **26**, 743-769. DOI: 10.1002/joc.1280, 2006.

Zeppetello, L. R. V., Battisti, D. S., Baker, M. B. The Physics of Heat Waves: What Causes Extremely High Summertime Temperatures?. *Journal of Climate*, **35**, 2231–2251. DOI: 10.1175/JCLI-D-21-0236.1, 2022.

Zhang, G., Wang, Z. North Atlantic Extratropical Rossby Wave Breaking during the Warm Season: Wave Life Cycle and Role of Diabatic Heating. *Monthly Weather Review*, **146** (3), 695-712. DOI: 10.1175/MWR-D-17-0204.1, 2018.